CrystEngComm

Accepted Manuscript

ROYAL SOCIETY OF CHEMISTRY

www.rsc.org/crystengcomm

CrystEngComm

ARTICLE

Comparison of Amorphous, Pseudohexagonal and Orthorhombic Nb_2O_5 for High-Rate Lithium Ion Insertion

Received 00th January 20xx,
Accepted 00th January 20xx

DOI: 10.1039/x0xx00000x

www.rsc.org/

Shuang Li,[ab] Qian Xu,[c] Evan Uchaker,[b] Xi Cao,[b] Guozhong Cao*[b]

Amorphous, pseudohexagonal and orthorhombic Nb_2O_5 nanoparticles were synthesized using a facile and green sol-gel process followed by a thermal treatment at 450 ℃, 600 ℃ and 800 ℃ for 3 h in air, respectively. The resulting material has been subjected to a detailed experimental study on and comparison of structural, electrical and electrochemical properties. The experiments have demonstrated that the pseudohexagonal Nb_2O_5 (TT-Nb_2O_5) exhibited higher storage capacity, largely due to its high specific surface area and small crystallites, and better cycling performance than both amorphous Nb_2O_5 (a-Nb_2O_5) and orthorhombic Nb_2O_5 (T-Nb_2O_5); such experimental findings were found to be associated, and thus ascribed to possess the lower charge transfer resistance and higher lithium ion diffusion coefficient of TT-Nb_2O_5 than that of a-Nb_2O_5 and T-Nb_2O_5. This research contributes to a better fundamental understanding of the relationship between the crystal structure and crystallinity and electrochemical properties, particularly the Li-ion storage properties, and lead to a possible new advancement in the research field of lithium ion batteries and pseudocapacitors.

Introduction

Electrochemical energy storage devices have attracted considerable attention in powering future advanced communication equipment, portable electrics, electric vehicles and smart grid.[1-3] For electric vehicles (EVs), the current commercial lithium-ion batteries (LIBs) commonly using graphite as the anodes cannot be matched to the stringent requirements of high power density, because of poor rate performance and especially safety concerns.[4] Thus, to develop advanced electrode materials, which possess better safety characteristics and high rate become imperative. There are several promising candidates including silicon and tin-based compounds being actively studied as anodic materials for the next generation of batteries as they offer high lithium-ion storage capacities,[5-8] however, they suffer from huge volume change accompanied with lithium insertion and extraction.[9] Lithium titanate ($Li_4Ti_5O_{12}$) is another most noticeable anodic material under intensive study as it offers a high charge/discharge voltage of 1.55 V (vs. Li/Li^+), and very stable cyclic stability since there is a very little volume change during the lithium ion insertion and extraction; however, their lithium ion storage capacity is 170 mA h g^{-1} theoretically.[10] Niobium pentoxide (Nb_2O_5) is yet another anodic material attracted a lot of research attention lately, as it exhibits unique fast charge and discharge kinetics, more as pseudocapacitors.[11] It has been reported that the high rate is attributed to the fact that the lithium insertion and extraction is rate-limited by the capacitive effect, not by the lithium ion diffusion through the electrode.[12] Compared to commercial graphite anode, Nb_2O_5 exhibits a similar insertion/extraction voltage to $Li_4Ti_5O_{12}$, which is higher than the voltage 1 V (vs. Li/Li^+) of SEI formation and suppress lithium dendrite deposition on the surface of the anode.[13] In addition, Nb_2O_5 has a good theoretical lithium-ion storage capacity of 200 mA h g^{-1},[14] which leads to a higher energy density and makes a good candidate for niche applications.

Owing to its attractive physical properties, Nb_2O_5 has been extensively studied and applied for various technical applications such as electrochemical pseudocapacitors,[11, 12] gas sensors,[15] catalysts,[16] electrochromics[17] and solar cells.[17, 18] The electrochemical property of Nb_2O_5 was first investigated by Bard et al., who demonstrated that Nb_2O_5 exhibits lithium-ion intercalation property, which led the further research of Nb_2O_5 as an anode for lithium ion battery.[19, 20] In recent years, various nanostructures of Nb_2O_5 as electrodes for lithium ion batteries have been studied, such as nanotubes, nanowires, nanofibers and spherical nanoparticles.[14, 21-24] Some researches revealed Nb_2O_5-C composites and Ti- or Ta-substituted Nb_2O_5 possessed improved electrochemical properties.[25-27] Li intercalation properties of other Nb-based oxides are summarized in recent review paper.[28] Nb_2O_5 has many polymorphic forms, such as a-Nb_2O_5 (amorphous Nb_2O_5), TT-Nb_2O_5 (pseudo hexagonal Nb_2O_5), T-Nb_2O_5 (orthorhombic Nb_2O_5), and M-Nb_2O_5 (monoclinic Nb_2O_5), which can be obtained mainly through controlled thermal treatment. The study on the transition and structures of TT-Nb_2O_5, T-Nb_2O_5 and M-Nb_2O_5 phases have been discussed in literature.[29] In Kodama et al.'s work several

[a] School of Materials Science and Metallurgy, Northeastern University, Shenyang 110819, PR China
[b] Department of Materials Science and Engineering, University of Washington, Seattle, Washington 98195, United States
[c] State Key Laboratory of Advanced Special Steel, Shanghai University, Shanghai 200072, PR China
†Electronic Supplementary Information (ESI) available. See DOI: 10.1039/x0xx00000x

crystal forms of Nb_2O_5 and intercalation process were discussed mainly using in situ XAFS-XRD.[30] A. Le Viet et al. reported M-Nb_2O_5 exhibited the highest capacity compared with T-Nb_2O_5 and tetragonal Nb_2O_5, besides, heat treated M-Nb_2O_5 (1100 ^oC) in argon shows much enhanced discharge capacity of 192 mAh g^{-1} at 150 mA g^{-1} current density.[27] Recently, Kim et al. synthesized a-Nb_2O_5, TT-Nb_2O_5 and T-Nb_2O_5 by different methods, reported their rapid pseudocapacitive characteristics by drop cast Nb_2O_5 nanoscale powders onto steel foil as electrode.[11] Those researches have clearly indicated that Nb_2O_5 polymorphs are very promising lithium storage materials. What's more, fast transport kinetics is another important advantage with high power density for lithium ion batteries besides large capacity. Thus, more work based on a detailed comparison of structural, electrical and electrochemical properties of a-Nb_2O_5, TT-Nb_2O_5 and T-Nb_2O_5 phase materials applied in lithium-ion batteries become necessary.

This paper reports the synthesis of nanostructured Nb_2O_5 via a facile and green sol-gel processing with forced hydrolysis and condensation and investigated the electrochemical properties of amorphous, TT-Nb_2O_5 and T-Nb_2O_5 nanoparticles, aimed at achieving a better fundamental understanding of the relationship between the electrochemical properties, in particular Li-ion storage properties, and the crystal and nanostructures. Specifically, we introduced NH_4OH and H_2O_2 to the precursor solution to catalyze and promote rapid hydrolysis and condensation reactions. The resulting Nb_2O_5 nanoparticles are amorphous in nature and the subsequent annealing at elevated temperatures converted amorphous niobium pentoxide to pseudohexagonal phase and orthorhombic crystal. When evaluated as an anode material for lithium-ion batteries, the three Nb_2O_5 phases all showed very stable cycle performance, and the TT-Nb_2O_5 nanoparticles showed higher lithium ion storage capacity than both amorphous and T-Nb_2O_5. Compared with the results of T-Nb_2O_5 and M-Nb_2O_5 reported in literature, pseudohexagonal crystal has the advantage of low processing temperature which can save energy in material processing.

Experimental method

Materials Synthesis

a-Nb_2O_5, TT-Nb_2O_5 and T-Nb_2O_5 nanoparticles were synthesized via a facile sol-gel processing followed by annealing in air at 450 ℃, 600 ℃ and 800 ℃, respectively. In a typical reaction, 1g of $NbCl_5$ was dissolved into 2 ml of ethanol, and a clear yellow $NbCl_5$ EtOH solution was formed. White precipitation was subsequently obtained from this solution by drop wise addition of 5% dilute ammonia, and the pH value was tuned at 7.[31] The precipitate was isolated from the solution and washed four times by centrifugation at 6000 rpm with deionized water. Then 4 ml of 30 wt. % hydrogen peroxide aqueous was added into the precipitate. The mixture was stirred for 5 minutes under ice-bath, and then a transparent yellow sol was obtained. This sol was dried in oven at 70 ℃ for 24 hours and then clear yellow xerogel was obtained. The xerogel was grinded into white particles and then annealed at ambient atmosphere at 450 ℃ (a-Nb_2O_5), 600 ℃ (TT-Nb_2O_5) and 800 ℃ (T-Nb_2O_5) for 3 hours, respectively.

Materials Characterization

The crystalline structure of the particles obtained was characterized by X-ray diffraction (XRD, D8 Bruker X-ray diffractometer with Cu-Kα radiation (λ=1.5418 Å)) within the range of 10°- 70° (2θ). X-ray photoelectron spectroscopy (XPS) analysis was performed using a VG Multilab 2000 with Al Ka as the X-ray source. The accelerating voltage and current were 40 kV and 40 mA, respectively. Scanning electron microscopy (SEM, JEOL, JSM-7000F) and transmission electron microscopy (TEM, FEI, Tecnai G2 F20) were used to examine the morphology and microstructure of the as prepared samples. Thermogravimetric analysis (TGA) was performed on a TG instrument (NET ZSCH STA 409C). Nitrogen adsorption-desorption isotherms were measured using Quantachrome NOVA 4200e system. Samples were degassed at 250 ℃ overnight under vacuum prior to measurements. The specific surface area and micropore volumes were determined by multipoint Brunauer-Emmett-Teller (BET), t-method, and Barret-Joyner-Halenda (BJH) desorption analyses, respectively.

Electrochemical Property Measurement

The electrochemical performances of the Nb_2O_5 polymorphs were tested in coin-type cells, which were assembled using as-prepared samples in an argon-filled glove-box (Innovative Technology, IL-2GB). The as-prepared active materials were mixed and ground with poly (vinylidene fluoride) (PVDF, sigma-Aldrich) as a binder and super P conductive carbon (TIMCAL Graphite & Carbon) as the conductive assistant materials at a respective weight ratio of 70:20:10 in a N-methy1-2-pyrrolidone (NMP, Alfa Aesar) solution. The as-prepared mixture was uniformly spread and pressed on to aluminum foil and dried in a vacuum oven at 80 ℃ overnight as the working electrode. The mass of the active material is approximately 0.5 mg. Pure lithium foil was used as the counter and reference electrodes. A polypropylene membrane film (Celgard 2400) was used as the separator. 1 M $LiPF_6$ in ethylene carbonate (EC)/dimethyl carbonate (DMC) was used as electrolyte. Galvanostatic charge/discharge measurements were performed in the voltage range of 1.2 to 3.0 V (vs Li/Li^+) under different current densities. Cyclic voltammetry (CV) was conducted on an electrochemical analyzer (CH Instruments, model 605C) in the voltage range of 1.2 to 3.0 V (vs Li/Li^+) at a scan rate of 0.2 mV s^{-1}. Electrochemical impedance spectroscopies (EIS) were performed on the Solartron 1287A in conjunction with a Solartron 1260FRA/impedance analyzer with amplitude of 5.0 mV in the frequency range from 100 kHz to 0.1 Hz. The half-cells were tested at various current rates based on the weight of the active material.

Results and Discussion

When $NbCl_5$ was dissolved into absolute ethanol, the following reaction would occur, leading to the formation of niobium chloride ethoxide: [32]

$$NbCl_5 + x\ CH_3CH_2OH \rightarrow NbCl_{5-x}(CH_3CH_2O)_x + x\ HCl \quad (1)$$

Continued stirring would allow the partial removal of HCl through evaporation, promoting the reaction (1) further, and also the absorption of H_2O from air, resulting in partial hydrolysis:

$$NbCl_{5-x}(CH_3CH_2O)_x + y\ H_2O \rightarrow Nb(CH_3CH_2O, OH)_5 + 5\text{-}x\ HCl + y\text{+}x\text{-}5\ HOCH_2CH_3 \quad (2)$$

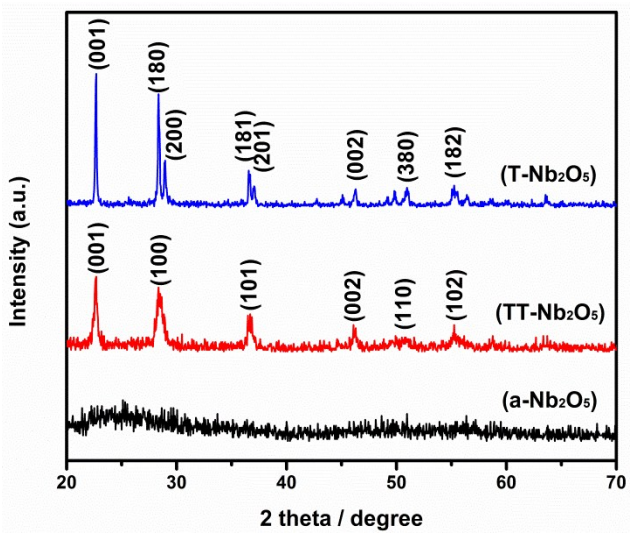

Fig. 1 XRD patterns of Nb_2O_5 polymorphs annealed in air for 3 hours under different temperatures: (a-Nb_2O_5): 450 ℃; (TT-Nb_2O_5): 600 ℃; (T-Nb_2O_5): 800 ℃.

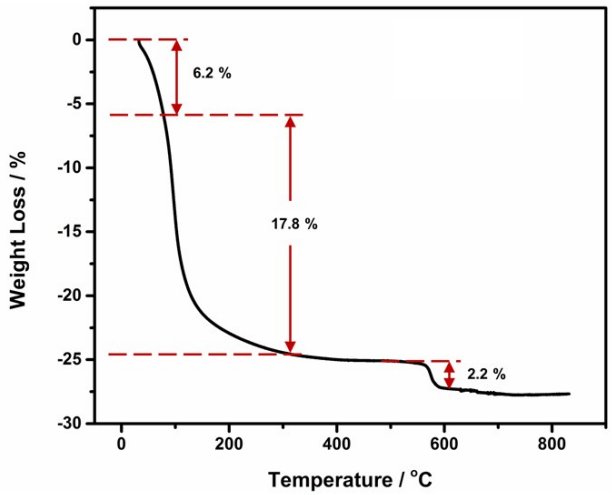

Fig. 2 TGA curve of pure Nb_2O_5 xerogel from 30 ℃ to 830 ℃ at a rate of 10 ℃ min^{-1}.

When NH_4OH was subsequently added, it reacts with HCl, increases the pH value, and promotes the hydrolysis and condensation reactions of niobium alkoxide as a catalyst, and the white precipitate of $Nb(OH)_5$ was subsequently obtained:

$$NH_4OH + HCl \rightarrow NH_4Cl + H_2O \quad (3)$$

$$Nb(CH_3CH_2O, OH)_5 + 5\ H_2O \rightarrow Nb(OH)_5 + HOCH_2CH_3 \quad (4)$$

NH_4Cl is a white precipitate in ethanol.[32] However, in the present work no NH_4Cl precipitant was observed, probably due to the low percentage of ethanol.

Collectively, the addition of NH_4OH to the niobium oxide sol is to promote both hydrolysis and condensation reaction, and consequently result in rapid nucleation process with a high density of nuclei of narrow size distribution. The addition of H_2O_2 resolved the precipitate and turned the colour from ivory to yellow, when dried in oven at 70 ℃, the release of by-product, oxygen gas, benefits the nucleation process as well. The release and removal of oxygen gas bubbles from the sol helped homogenizing the concentration and temperature of the sol so as to ensure the uniform size of nanoparticles, and also prevented the possible formation of agglomeration of nanoparticles. The SEM images as shown in Figure 3b and Figure 3d have demonstrated the difference between the as-synthesized Nb_2O_5 nanoparticles synthesized with and without the addition of H_2O_2 through a sol-gel processing under otherwise the same conditions. The Nb_2O_5 nanoparticles synthesized with the addition of H_2O_2 are smaller and are better dispersed, i.e., less aggregated.

Through thermal treatment process different Nb_2O_5 polymorphs were formed using the method above-mentioned. The crystalline structure and crystallinity of the as-prepared materials annealed at different temperatures are detected by XRD, the results are displayed in Figure 1. The intensity and shape of the diffraction peaks vary greatly while the annealing temperature changes. As-prepared Nb_2O_5 xerogel was amorphous. For 450 ℃ annealing temperature the diffraction peaks are mild, and the pattern is close to the shape of amorphous. That might be the particles could not change into crystal very well under this annealing temperature. When annealing temperature is 600 ℃, Nb_2O_5 of pseudohexagonal crystal (TT-Nb_2O_5) is formed. All the diffraction peaks are clear and in good agreement with the TT-Nb_2O_5 (space group: P6/mmm, JCPDS: 28-317), though the intensity of the peaks is weak, the peaks are broad and the signal to noise ratio is low, all are indicative of small crystal size and/or poor crystallinity. The average crystallite size of TT-Nb_2O_5 was calculated to be of approximately 22.5 nm using Scherer equation. Between 600 ℃ and 800 ℃ there is a crystal transition. Since when the annealing temperature rises to 800 ℃ the diffraction peaks are consistent with the peaks of orthorhombic Nb_2O_5 (T-Nb_2O_5, space group: Pbam, JCPDS: 30-0873). The average crystallite size was estimated to be of ~ 113.3 nm by Scherer equation. The crystallite of T-phase is significantly larger than that of TT-Nb_2O_5, as the annealing temperature is much higher. The high intensity and narrow width of T-Nb_2O_5 peaks imply it crystallized very well under the annealing temperature 800 ℃.

In order to study the crystalline water loss and the crystal transition during the annealing process, TGA was carried out in flowing air from 30 ℃ to 830 ℃ with a heating rate of 10 ℃ min^{-1} and the TGA curve of the pure Nb_2O_5 xerogel is shown in Figure 2. From the TGA curve we can see the weight loss started with a mild curve from room temperature to around 90 ℃ which is supposed to be the physically adsorbed water molecules. A large mass loss of about 20% from 90 to 300 ℃ mainly involves fragments of organic molecules (C_xH_y) and HCl, it is attributed to the building up of the inorganic amorphous network.[33] The lower mass loss of 2.2% located at around 580 ℃ accompanies the crystallization process is due to a transformation from uncharacterized hydrate niobium pentoxide, also known as niobic acid or columbic acid ($Nb_2O_5 \cdot nH_2O$) gel to Nb_2O_5 crystal (pseudohexagonal).[31] From 600 ℃ to 800 ℃ the weight loss is less than 0.5%. That means although the morphology variation is significant and the crystal structure changed from pseudohexagonal to orthorhombic, the weight loss is inconspicuous. That result agrees well to the works published in literature.[17, 24] In their works no appreciable weight loss or

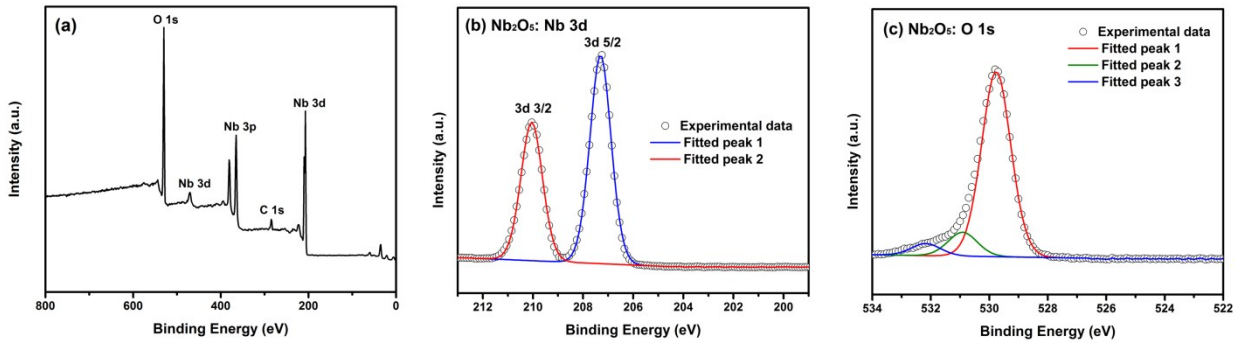

Fig. 3 XPS spectrum of (a) wide survey of TT-Nb_2O_5 nanoparticles, (b) the zone-in Nb 3d spectrum, (c) the zone-in O 1s spectrum.

crystallization peaks (from their differential thermal analysis results) were observed for the crystal structure change from pseudohexagonal to orthorhombic.

XPS analyses were carried out in the region of 0–800 eV to elucidate the chemical composition. Figure 3 shows the typical XPS spectra taken from the niobium and oxygen regions of TT-Nb_2O_5. The binding energy scales of the spectra were calibrated by assigning the most intense C 1s peak a binding energy of 284.8 eV. Figure 3a reveals that the sample contains the Nb, O and C elements. In Figure 3b, the Nb 3d level binding energies of TT-Nb_2O_5 were 207.3 and 210.0 eV, which are attributed to the doublet Nb $3d_{5/2}$ and Nb $3d_{3/2}$ core levels of Nb^{5+}, respectively. These binding energies of Nb^{5+} ions are in close agreement with the values reported.[34, 35] Figure 3c shows the binding energies of O 1s peaks. Among these peaks the sharp one located at 529.6 eV and the low one located at 531.9 eV are signed to O^{2-} in Nb-oxides and surface oxygen, respectively.[24] Another O 1s peak located at 530.7 eV could be the peak of C-O, some possible residual groups.

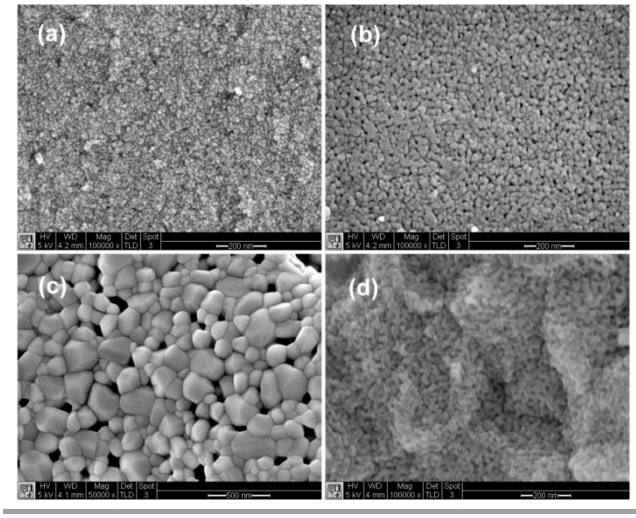

Fig. 4 SEM images of Nb_2O_5 particles obtained from (a) a-Nb_2O_5, (b) with H_2O_2 annealed at 600 ℃, (c) with H_2O_2 annealed at 800 ℃ in air for 3 h, (d) no H_2O_2 added and annealed at 600 ℃.

SEM and TEM were carried out to investigate the microstructure and morphology of the as-synthesized samples. As shown in Figure 4a, 450 ℃ annealed a-Nb_2O_5 has smaller particle size, better dispersion and higher porosity. From the Figure 4b it can be clearly seen that the particle is formed homogenously after annealed at 600 ℃ for 3 h in air, and the TT-Nb_2O_5 have a narrow size distribution at around 20 nm. When the powders annealed at 800 ℃ (Figure 4c), larger size T-Nb_2O_5 particles at around 100 nm were obtained. That means the temperature rise not only modified the crystalline phase but also increased the size. Figure 4d presents the SEM images of the Nb_2O_5 particles without hydrogen peroxide added annealed at 600 ℃ for 3 h in air, in this image, connections between particles can be found. Compared Figure 4b and Figure 4d it can be clearly seen that the particles in Figure 4b have much better uniform dispersion, that also proved the addition of H_2O_2 can improve the dispersity of Nb_2O_5 nano-particles. The high resolution TEM images provide more detailed structural information as seen in Figure 5. Compared to a-Nb_2O_5 shown in Figure 5a the lattice fringes of the TT-Nb_2O_5 and T-Nb_2O_5 particles can be clearly observed in Figure 5b and Figure 5c, suggesting the presence of a well-defined crystal structure. The periodic lattice fringe spaces in Figure 5b were found to be 0.32 and 0.25 nm corresponding to the interplanar spacings of the (100) and the (101) planes, respectively, for pseudohexagonal Nb_2O_5 (JCPDS: 28-317); in Figure 5c the periodic lattice fringe spaces were 0.38 and 0.31 nm which agreed well to the interplanar spacings of the (001) and the (180) planes. These results further corroborate the findings from XRD.

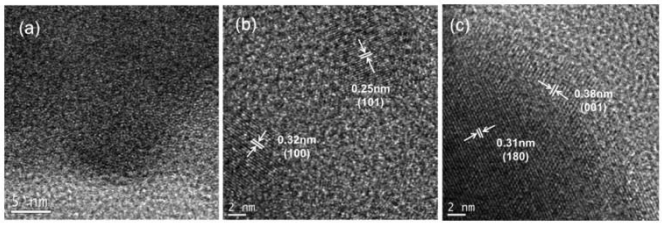

Fig. 5 High-resolution TEM images of (a) a-Nb_2O_5 (b) TT-Nb_2O_5 (c) T-Nb_2O_5

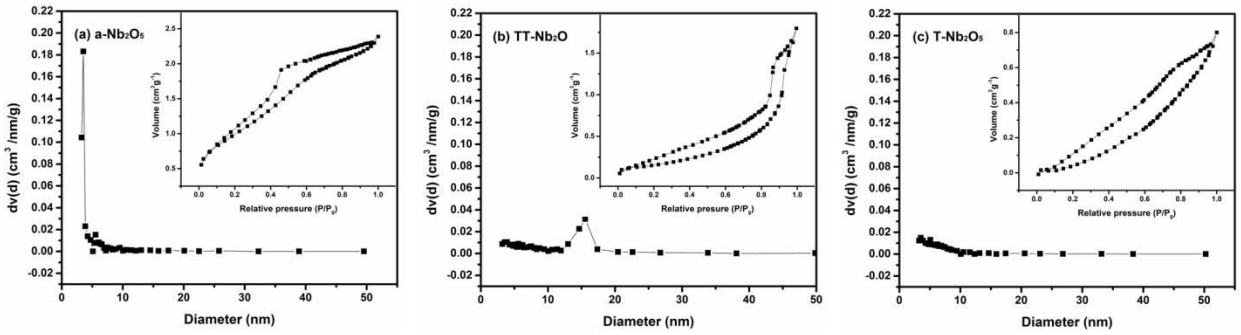

Fig. 6 BJH desorption pore size distribution for the as synthesized Nb_2O_5 polymorphs (a) a-Nb_2O_5 (b) TT-Nb_2O_5 (b) T-Nb_2O_5 (inset: N_2 adsorption-desorption isotherm)

The presence of the pores and the porous distribution of the Nb_2O_5 polymorphs were confirmed by the corresponding nitrogen sorption isotherms and Barrett-Joyner-Halenda (BJH) desorption analyses which shown in Figure 6. The results in Figure 6a indicated that the pore size of a-Nb_2O_5 centrally distributed at 3.5 nm which was the only mesoporous distribution can be found, and the Brunauer-Emmett-Teller (BET) derived surface area was determined to be 129.6 m^2g^{-1}. Within the TT-Nb_2O_5 sample the majority of pores are around 15 nm (Figure 6b), and it exhibits very narrow pore size distribution. The BET surface area of TT-Nb_2O_5 was 57.8 $m^2\ g^{-1}$, which is a reasonable value providing excellent channels and cavities for complete and homogeneous Li^+ diffusion and intercalation throughout the material.[36] For the T-Nb_2O_5 sample (Figure 6c), no obvious pore size distribution was observed in our study, the peak of pore size distributions at 3.5 and 5 nm are very weak. The surface area of T-Nb_2O_5 turns to be only 43.0 $m^2\ g^{-1}$, which is far less than a-Nb_2O_5 and TT-Nb_2O_5.

In order to investigate the storage properties of the Nb_2O_5 polymorphs, CV curves, galvanostatic charge/discharge measurements and electrochemical impedance analysis have been performed. The first, second and fifth CV curves of a-Nb_2O_5, TT-Nb_2O_5 and T-Nb_2O_5 samples collected at a scan rate of 0.2 mV s^{-1} in the voltage range of 1.2-3.0 V (vs Li/Li^+) were shown in Figure 7. The three Nb_2O_5 polymorphs all showed good repeatability. For the T-Nb_2O_5 (Figure 7c), the current response of the cathodic sweep increases greatly below 2.1 V (vs Li/Li^+), and two obvious reduction reactions located at 1.72 and 1.54 V correspond to the valence variation during the intercalation process. On the reversal sweep, an ambiguous broad peak at 1.82 V reveals that the continuous variation from Nb^{4+} back to Nb^{5+} takes place during the redox process.[30] The cathodic and anodic peaks of TT-Nb_2O_5 (Figure 7b) are broad and located at 1.5 V and 1.85 V, respectively. In contrast, the CV peaks of a-Nb_2O_5 material (Figure 7a) are very obscure except for the first cycle which exhibits a small reduction peak at 2.0 V and a wide shift of CV curve to the other cycles.

Figure 8 displays the charge-discharge profiles of the Nb_2O_5 polymorphs for the first three cycles at a current rate of 10 mA g^{-1} in the voltage rang of 1.2-3.0 V (vs Li/Li^+). As shown in Figure 8a, a-Nb_2O_5 was exhibited an initial discharge capacity of 291 mA h g^{-1}, but dropped to 150 mAh g^{-1}, nearly half to the first discharge capacity, with the second cycle. Similarly, TT-Nb_2O_5 and T-Nb_2O_5 showed a decrease in capacity following the first cycle, however, the proportion of reversible capacity in the second cycle is much larger than a-Nb_2O_5, at around 80% for both TT-Nb_2O_5 and T-Nb_2O_5. a-Nb_2O_5 exhibited the highest initial discharge capacity and the largest decay in the second cycle. That agrees well with CV curves in Figure 7a, which possesses a wide shift between first and second reductive curves, suggesting a large amount of capacity decrease. In contrast, the CV curves for crystalline Nb_2O_5 (Figure 7b, 7c) are more reversible between the first two cycles. In addition, from Figure 7a a mild reductive peak located at 2.0 V revealed some irreversible chemical reaction with Li could exist.[37] On the other hand, from the TGA analysis in Figure 2, a-Nb_2O_5 should contain the

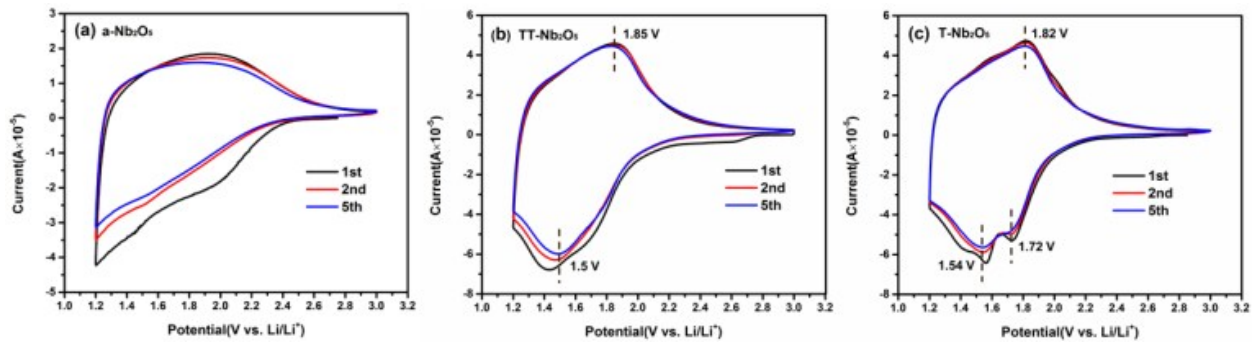

Fig. 7 CV curves of Nb_2O_5 polymorphs electrode materials (a) a-Nb_2O_5 (b) TT-Nb_2O_5 (c) T-Nb_2O_5 measured in the voltage rang of 1.2-3.0 V (vs Li/Li^+) with a scan rate of 0.2 mV s^{-1}.

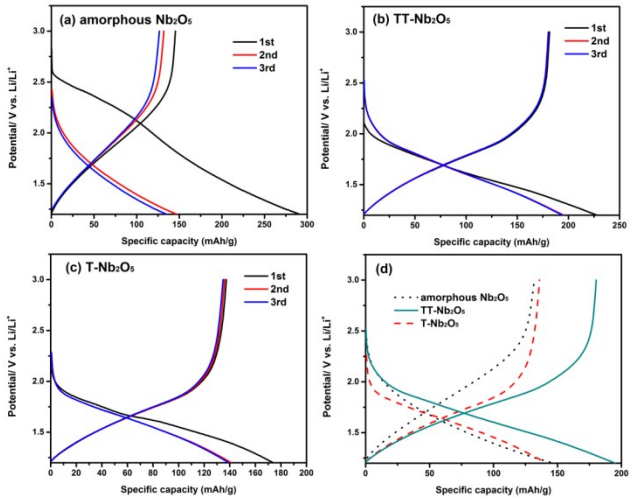

Fig. 8 First three discharge and charge curves of the samples at a current density of 10 mA g^{-1} in a half-cell: (a) a-Nb_2O_5, (b) TT-Nb_2O_5, (c) T-Nb_2O_5, (d) a comparison of the second cycle curves of three samples.

loss of 2.2% located at 580 ℃ in form of hydroxyl group (O-H), which could bring undesirable irreversible electrochemical reaction with Li in initial cycle.[38, 39] The existence of O-H in amorphous materials has been proved in previous reports, and it is also not detected in fully crystallized material.[40] From the figures of TT-Nb_2O_5 and T-Nb_2O_5, curves of similar shape can be found which have no plateaus on, that implies the charge and discharge processes of TT-Nb_2O_5 and T-Nb_2O_5 samples are very fast, which are in a good agreement with the character of pseudocapacitance.[12, 41] Among three samples, TT-Nb_2O_5 shows the highest reversible charge/discharge capacities of about 190 mA h g^{-1} which is much higher than the capacity of 110 mA h g^{-1} reported by Kodama et al.,[30] such a high capacity might be the results of high specific surface area and the nanosized crystallites. For larger sized T-Nb_2O_5 the reversible charge/discharge capacities in the present study is similar to the results reported in literature.[27] From here we see that the difference is probably because the nanoscale TT-Nb_2O_5 particles obtained in this sol-gel method can provide larger surface area for Li^+ de/intercalation and thereby improve the capacity.[3] More capacities under different charge rate and stability will be shown in Figure 9.

The rate performance of a-Nb_2O_5, TT-Nb_2O_5 and T-Nb_2O_5 samples at various charge-discharge rates are compared in Figure 9. The charge-discharge curves show that all these three Nb_2O_5 polymorphs have very regular performance. There is no obvious fading can be found after 120 cycles. Among these samples, TT-Nb_2O_5 electrode shows the highest capacity at each current rate. The discharge capacities measured in the voltage window from 1.2 V to 3 V are 191, 164, 146, 130, 122 and 114 mA h g^{-1} at the current densities of 50, 100, 200, 300, 400 and 500 mA g^{-1}, respectively. More important, when the current rate is reversed back to 100 mA g^{-1} after different rates testing above mentioned, the discharge capacity went back up to 172mA h g^{-1} which is even higher to the initial discharge capacity at the same rate (164 mA h g^{-1}) .That implies the decline of capacity at large rate is limited. After 120

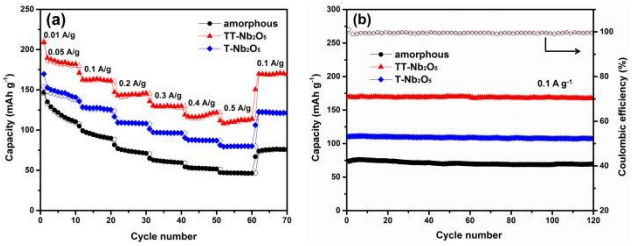

Fig. 9 (a) Rate capability of Nb_2O_5 polymorphs at different current densities, (b) Cycling performance of Nb_2O_5 polymorphs at current densities of 100 mA g^{-1}.

charge-discharge cycles TT-Nb_2O_5 electrode demonstrated specific discharge capacity of 170 mA h g^{-1} at a current density of 100 mA g^{-1}, which is close to the capacity of the high temperature phase, the pristine monoclinic phase, in report.[27] Possessing a relatively stable charge-discharge performance, T-Nb_2O_5 electrode showed much lower capacities than TT-Nb_2O_5 electrode at each current rate mentioned above, and its specific discharge capacity was stable at 110 mA h g^{-1} during 120 charge-discharge cycles. Apparent fading was observed during the first 20 cycles in the rate capability of a-Nb_2O_5 electrode. What's more, the a-Nb_2O_5 electrode showed even lower capacities at different current rates, especially, when the current rate was 500 mA g^{-1} it fell to as low as 50 mA h g^{-1}. The intercalation reaction is sensitive to doping, preparation temperature and particle size were also documented in TiO_2 as well as other systems.[42] It should be noted that research on other transition-metal oxides such as Fe_2O_3 and MnO_x, showed that amorphous phase possessed much enhanced performance than that of crystalline counterparty.[37, 43] The reason of their results has been explained to their unique structures which are beneficial for lithium ion storage. When compare their CV curves between amorphous and crystalline, only small changes could be found such as slight shift of peak location, peak intensity or/and peak width. However, the main CV curves between amorphous and crystalline are very similar, which implies that for these two materials there are not significant mechanism differences of lithiation process caused by changing crystalline into amorphous. In contrast, our CV results reveal that there are either some mechanism changes in lithiation process or some capacity deficiency because the CV curve of a-Nb_2O_5 significantly changed with a lack of redox reaction peaks compared with crystalline Nb_2O_5. Those different lithiation mechanisms may explain the result that crystalline Nb_2O_5 showed better lithium ion storage properties than that of a-Nb_2O_5 in the present work.

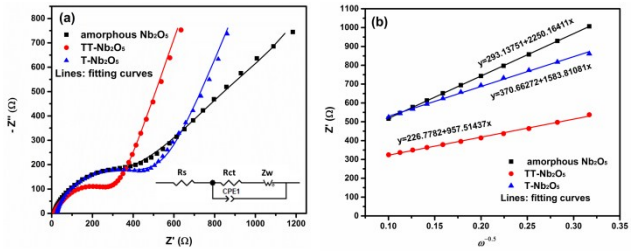

Fig. 10 (a) EIS plots of Nb_2O_5 polymorphs at 25 ℃ and (b) the Z'-$\omega^{-0.5}$ plots in the low frequency range.

Table 1. Summary of BET and EIS results of Nb_2O_5 polymorphs.

Samples	Specific surface area m^2g^{-1}	Pore size nm	R_e Ω	$R_{(sf+ct)}$ Ω	Diffusion coefficients $cm^2\ s^{-1}$
a-Nb_2O_5	130	3.5	12.09	332.9	1.39×10^{-21}
TT-Nb_2O_5	58	15	12.38	261.5	3.86×10^{-20}
T-Nb_2O_5	43	-	12.75	400.9	2.56×10^{-20}

For the sake of comparison of the electrochemical properties of M-Nb_2O_5, Nb_2O_5 precursor was annealed at 1100 ^oC in air for 3 h and the resulting monoclinic phase was obtained as confirmed by XRD patterns shown in Figure S1a (ESI†). The electrochemical properties (shown in Figure S1, EIS†) turned out to be in good agreement with that has been reported in literature.[24] More specifically, discharge-charge profiles showed a clear discharge plateau at a potential around 1.65 V, it is the same as reported in literature.[24] However, the CV curves were slightly different in appearance, which was likely due to the high scan rate used in the current study as compared with that in literature (0.2 mV s^{-1} vs 0.058 mV s^{-1}). The resulting M-Nb_2O_5 demonstrated a high reversible capacity of 185 mA h g^{-1} at a low rate of 10 mA g^{-1}. The capacity was found to be 120 mA h g^{-1} at a high rate of 100 mA g^{-1}. The M-Nb_2O_5 in the current investigation possessed a smaller capacity as compared to TT-Nb_2O_5.

To investigate the electrochemical kinetics of Li^+ intercalation/deintercalation process within Nb_2O_5 polymorphous electrode, EIS measurement was performed over a frequency range of 100 kHz to 0.1 Hz with the results shown in Figure 10. The impedance data were recorded for fresh cells after 5 discharge-charge cycles at the current rate of 0.5 C. The voltage was 3.0 V under the charging status. As shown in the figure, the Nyquist plot of a-Nb_2O_5, TT-Nb_2O_5 and T-Nb_2O_5 electrodes display a single semicircle in the high frequency region and a straight line in the low frequency range. The EIS was simulated by Z-view software using the equivalent circuit shown in the inset.[35, 44, 45] It consists of the solution resistance (R_s), charge-transfer (R_{ct}) resistance, a constant phase element (CPE_1) and diffusional component Warburg impedance (Z_w). The semicircle at the high frequency region associates with the charge transfer resistance (R_{ct}).[46, 47] The fitted R_{ct} values are 332.9 Ω, 261.5 Ω and 400.9 Ω for a-Nb_2O_5, TT-Nb_2O_5 and T-Nb_2O_5 electrodes, respectively.

With the lowest R_{ct} value TT-Nb_2O_5 demonstrates better electrical conductivity, which can be a reason for its higher capacity and cycling performance. A straight line on the low frequency stands for the Warburg impedance.[48] The diffusion coefficient of lithium ion, D_{Li}, as one of the main kinetic factors in the rate-determining step of the intercalation process can be calculated from several techniques, such as CV, EIS, and galvanostatic intermittent titration technique (GITT). These testing methods are based on their respective formula derived by Fick's law and Nernst equation. The differences are mostly come from adopting different boundary conditions, initial conditions and numerical analysis methods. The CV technique can provide quantitative information on the electrode process, and the reversibility, stability and phase transformations during intercalation and de-intercalation reactions. The GITT is established to be a reliable technique to investigate the D_{Li} with highly resolved data for intercalation compounds of varying lithium content or potential. The EIS is also a powerful technique to calculate the D_{Li} due to the fact that the low frequency Warburg contribution of the impedance response is directly related to the lithium-ion diffusion process in an electrode material.[49] Slight differences in diffusion coefficient may exist when different test techniques were applied, however, D_{Li} obtained from the same technique can still be used to analyze and compare different systems and different electrode materials. The D_{Li} here was calculated from the plots in the low-frequency region. The equation for the calculation of D_{Li} values by EIS can be expressed as follows:[50-52]

$$Z' = R_b + R_{ct} + \sigma\omega^{-0.5} \quad (6)$$

$$D_{Li} = \frac{(RT)^2}{2(An^2F^2C_{Li}\sigma)^2} \quad (7)$$

where *T* is the absolute temperature, *R* is the gas constant, *n* is the number of electrons per molecule during oxidization, *A* is the surface area, F is Faraday's constant, C_{Li} is the concentration of lithium ion, ω is the angular frequency, and σ is the Warburg factor, which has a relationship with Z'. The Z'-$\omega^{-0.5}$ plots are presented in Figure 10b.

Based on the fitting linear equation in Figure 10b, the Li ion diffusion coefficients of a-Nb_2O_5, TT-Nb_2O_5 and T-Nb_2O_5 were calculated and the results are 1.39×10^{-21} $cm^2\ s^{-1}$, 3.86×10^{-20} $cm^2\ s^{-1}$ and 2.56×10^{-20} $cm^2\ s^{-1}$, respectively. The lower surface film and charge transfer resistance, the higher Li ion diffusion coefficient and electrical conductivity of TT-Nb_2O_5 electrode lead to its superior rate capabilities and other electrochemical properties. Table 1 is a summary of BET and EIS data of three Nb_2O_5 polymorphs. In general, larger surface area provides more reaction sites, shorter diffusion paths for ionic transport and electronic conduction, leading to higher power density.[53] In this work, the crystallinity and crystal structure exhibits an obvious influence on the electrical conductivity as well as the ionic diffusivity. The surface area of a-Nb_2O_5 is twice as large as TT-Nb_2O_5, however, the resistance is lower than TT-Nb_2O_5. That means during the process of crystal phase transition between amorphous and TT phase, better crystallinity significantly reduced the value of resistance. In general, better crystallinity means more ordered arrangement of ions and fewer defects, which collectively offer more order passage for charge and mass transport, leading to fast diffusion and high conductivity (low resistance). During the transformation from amorphous to TT phase, the crystals tend to be more perfect. When the crystal phase transformed from TT phase to T phase, although crystallinity improved to some extent, the particle size became larger, too. Larger particle size causes long diffusion paths for ionic transport which can be a reason for high resistance.

Conclusions

a-Nb_2O_5, TT-Nb_2O_5 and T-Nb_2O_5 nanoparticles were synthesized using a facile and environmentally benign sol-gel process followed by a thermal treatment. The size of TT-Nb_2O_5 particles is around 20 nm, which is much smaller than T-Nb_2O_5 which is around 100 nm. The Nb_2O_5 nanoparticles synthesized with the addition of H_2O_2 are

smaller and are better dispersed. When evaluated as an anode material for lithium-ion batteries, a-Nb_2O_5, TT-Nb_2O_5 and T-Nb_2O_5 electrodes demonstrated specific discharge capacities of 149 mA h g^{-1}, 191 mA h g^{-1} and 152 mA h g^{-1}, respectively at a current density of 50 mA g^{-1}. The large capacity of TT-Nb_2O_5 is most likely attributable to its large specific surface area. All these three Nb_2O_5 polymorphs have very stable cyclic stability within 120 cycles at a current density of 100 mA g^{-1}. In addition to its large capacity, the TT-Nb_2O_5 possesses lower charge transfer resistance, higher lithium ion diffusion coefficient and electrical conductivity than both a-Nb_2O_5 and T-Nb_2O_5, which might be ascribed to its favourable crystal structure.

Acknowledgements

Shuang Li would like to acknowledge the financial support as a scholarship from the China Scholarship Council (CSC) for her Ph.D. study at the University of Washington. This research was also financially supported in part by the National Science Foundation (NSF, DMR-1505902).

Notes and references

1. M. Armand and J. M. Tarascon, *Nature*, 2008, **451**, 652-657.
2. C. Liu, F. Li, L.-P. Ma and H.-M. Cheng, *Adv. Mater.*, 2010, **22**, E28-E62.
3. Q. Zhang, E. Uchaker, S. L. Candelaria and G. Cao, *Chem. Soc. Rev.*, 2013, **42**, 3127-3171.
4. M. M. Rahman, R. A. Rani, A. Z. Sadek, A. S. Zoolfakar, M. R. Field, T. Ramireddy, K. Kalantar-zadeh and Y. Chen, *J. Mater. Chem. A*, 2013, **1**, 11019-11025.
5. A. Magasinski, P. Dixon, B. Hertzberg, A. Kvit, J. Ayala and G. Yushin, *Nat Mater*, 2010, **9**, 353-358.
6. S.-H. Ng, J. Wang, D. Wexler, K. Konstantinov, Z.-P. Guo and H.-K. Liu, *Angew. Chem. Int. Ed.*, 2006, **45**, 6896-6899.
7. L.-F. Cui, Y. Yang, C.-M. Hsu and Y. Cui, *Nano Lett.*, 2009, **9**, 3370-3374.
8. J. Fan, T. Wang, C. Yu, B. Tu, Z. Jiang and D. Zhao, *Adv. Mater.*, 2004, **16**, 1432-1436.
9. S. D. Beattie, D. Larcher, M. Morcrette, B. Simon and J.-M. Tarascon, *J. Electrochem. Soc.*, 2008, **155**, A158-A163.
10. M. R. Jo, K. M. Nam, Y. Lee, K. Song, J. T. Park and Y.-M. Kang, *Chem. Comm.*, 2011, **47**, 11474-11476.
11. J. W. Kim, V. Augustyn and B. Dunn, *Adv. Energy Mater.*, 2012, **2**, 141-148.
12. A. Veronica, C. Jérémy, A. L. Michael, K. Jong Woung, T. Pierre-Louis, H. T. Sarah, D. A. Héctor, S. Patrice and D. Bruce, *Nature Mater.*, 2013, **12**, 518-522.
13. L. Shen, B. Ding, P. Nie, G. Cao and X. Zhang, *Adv. Energy Mater.*, 2013, **3**, 1484-1489.
14. M. Wei, Z.-m. Qi, M. Ichihara and H. Zhou, *Acta Mater.*, 2008, **56**, 2488-2494.
15. R. A. Rani, A. S. Zoolfakar, J. Z. Ou, M. R. Field, M. Austin and K. Kalantar-zadeh, *Sensors Actuat. B-Chem.*, 2013, **176**, 149-156.
16. D. Prasetyoko, Z. Ramli, S. Endud and H. Nur, *Mater. Chem. Phys.*, 2005, **93**, 443-449.
17. M. A. Aegerter, *Sol. Energy Mater. Sol. Cells*, 2001, **68**, 401-422.
18. A. Le Viet, R. Jose, M. Reddy, B. Chowdari and S. Ramakrishna, *J. Phys. Chem. C*, 2010, **114**, 21795-21800.
19. B. Reichman and A. J. Bard, *J. Electrochem. Soc.*, 1980, **127**, 241-242.
20. B. Reichman and A. J. Bard, *J. Electrochem. Soc.*, 1981, **128**, 344-346.
21. C. Yan and D. Xue, *Adv. Mater.*, 2008, **20**, 1055-1058.
22. M. V. Reddy, R. Jose, A. Le Viet, K. I. Ozoemena, B. V. R. Chowdari and S. Ramakrishna, *Electrochim. Acta*, 2014, **128**, 198-202.
23. M. Sasidharan, N. Gunawardhana, M. Yoshio and K. Nakashima, *Mater. Res. Bull.*, 2012, **47**, 2161-2164.
24. A. L. Viet, M. V. Reddy, R. Jose, B. V. R. Chowdari and S. Ramakrishna, *J. Phys. Chem. C*, 2009, **114**, 664-671.
25. B. Guo, X. Yu, X.-G. Sun, M. Chi, Z.-A. Qiao, J. Liu, Y.-S. Hu, X.-Q. Yang, J. B. Goodenough and S. Dai, *Energy Environ. Sci.*, 2014, **7**, 2220-2226.
26. G. Li, X. Wang and X. Ma, *J. Energy Chem.*, 2013, **22**, 357-362.
27. A. Le Viet, M. Reddy, R. Jose, B. Chowdari and S. Ramakrishna, *Electrochim. Acta*, 2011, **56**, 1518-1528.
28. M. Reddy, G. Subba Rao and B. Chowdari, *Chem. Rev.*, 2013, **113**, 5364-5457.
29. I. Nowak and M. Ziolek, *Chem. Rev.*, 1999, **99**, 3603-3624.
30. R. Kodama, Y. Terada, I. Nakai, S. Komaba and N. Kumagai, *J. Electrochem. Soc.*, 2006, **153**, A583-A588.
31. N. Uekawa, T. Kudo, F. Mori, Y. J. Wu and K. Kakegawa, *J. Colloid Interface Sci.*, 2003, **264**, 378-384.

32. C. J. Brinker and G. W. Scherer, *Sol-gel science: the physics and chemistry of sol-gel processing*, Academic press, 2013.
33. M. Schmitt and M. A. Aegerter, *Electrochim. Acta*, 2001, **46**, 2105-2111.
34. N. Özer, M. D. Rubin and C. M. Lampert, *Sol. Energy Mater. Sol. Cells*, 1996, **40**, 285-296.
35. S.-q. Guo, X. Zhang, Z. Zhou, G.-d. Gao and L. Liu, *J. Mater. Chem. A*, 2014, **2**, 9236-9243.
36. E. Uchaker, M. Gu, N. Zhou, Y. Li, C. Wang and G. Cao, *Small*, 2013, **9**, 3880-3886.
37. J. Guo, Q. Liu, C. Wang and M. R. Zachariah, *Adv. Funct. Mater.*, 2012, **22**, 803-811.
38. B. Xu, D. Qian, Z. Wang and Y. S. Meng, *Mater. Sci. Eng., R*, 2012, **73**, 51-65.
39. A. Kraytsberg and Y. Ein-Eli, *Adv. Energy Mate.*, 2012, 2, 922-939.
40. E. Uchaker, Y. Z. Zheng, S. Li, S. L. Candelaria, S. Hu and G. Z. Cao, *J. Mater. Chem. A*, 2014, **2**, 18208-18214.
41. V. Augustyn, P. Simon and B. Dunn, *Energy Environ. Sci.*, 2014, **7**, 1597-1614.
42. C. T. Cherian, M. Reddy, T. Magdaleno, C.-H. Sow, K. Ramanujachary, G. S. Rao and B. Chowdari, *CrystEngComm*, 2012, **14**, 978-986.
43. Y. Jiang, D. Zhang, Y. Li, T. Yuan, N. Bahlawane, C. Liang, W. Sun, Y. Lu and M. Yan, *Nano Energy*, 2014, **4**, 23-30.
44. P. Nithyadharseni, M. Reddy, B. Nalini, M. Kalpana and B. Chowdari, *Electrochim. Acta*, 2015, **161**, 261-268.
45. B. Das, M. Reddy, C. Krishnamoorthi, S. Tripathy, R. Mahendiran, G. S. Rao and B. Chowdari, *Electrochim. Acta*, 2009, **54**, 3360-3373.
46. S. Hu, F. Yin, E. Uchaker, W. Chen, M. Zhang, J. Zhou, Y. Qi and G. Cao, *J. Phys. Chem. C*, 2014, **118**, 24890-24897.
47. M. Umeda, K. Dokko, Y. Fujita, M. Mohamedi, I. Uchida and J. R. Selman, *Electrochim. Acta*, 2001, **47**, 885-890.
48. S. S. Zhang, K. Xu and T. R. Jow, *Electrochim. Acta*, 2004, **49**, 1057-1061.
49. X. Rui, N. Ding, J. Liu, C. Li and C. Chen, *Electrochim. Acta*, 2010, **55**, 2384-2390.
50. Y.-F. Deng, S.-X. Zhao, Y.-H. Xu and C.-W. Nan, *J. Mater. Chem. A*, 2014, **2**, 18889-18897.
51. Q. Cao, H. P. Zhang, G. J. Wang, Q. Xia, Y. P. Wu and H. Q. Wu, *Electrochem. Comm.*, 2007, **9**, 1228-1232.
52. H. Song, Y. Liu, C. Zhang, C. Liu and G. Cao, *J. Mater. Chem. A*, 2015, **3**, 3547-3558.
53. G. Cao, *Synthesis, Properties and Applications*, World Scientific, 2004.

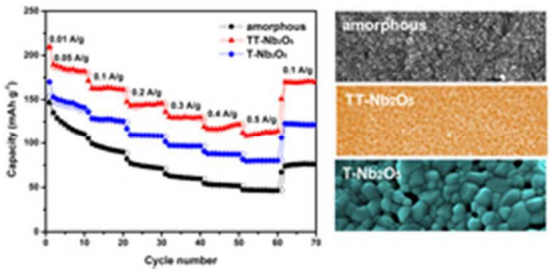

23x11mm (300 x 300 DPI)